Thiol Ligand-Induced Transformation of $Au_{38}(SC_2H_4Ph)_{24}$ to $Au_{36}(SPh\text{-}t\text{-}Bu)_{24}$

Chenjie Zeng,[†] Chunyan Liu,[‡] Yong Pei,[‡] and Rongchao Jin[†,*]

[†]Department of Chemistry, Carnegie Mellon University, 4400 Fifth Avenue, Pittsburgh, Pennsylvania 15213, United States, and [‡]Department of Chemistry, Key Laboratory of Environmentally Friendly Chemistry and Applications of Ministry of Education, Xiangtan University, Hunan Province 411105, People's Republic of China

ABSTRACT We report a disproportionation mechanism identified in the transformation of rod-like biicosahedral $Au_{38}(SCH_2CH_2Ph)_{24}$ to tetrahedral $Au_{36}(TBBT)_{24}$ nanoclusters. Time-dependent mass spectrometry and optical spectroscopy analyses unambiguously map out the detailed size-conversion pathway. The ligand exchange of $Au_{38}(SCH_2CH_2Ph)_{24}$ with bulkier 4-*tert*-butylbenzenethiol (TBBT) until a certain extent starts to trigger structural distortion of the initial biicosahedral $Au_{38}(SCH_2CH_2Ph)_{24}$ structure, leading to the release of two Au atoms and eventually the $Au_{36}(TBBT)_{24}$ nanocluster with a tetrahedral structure, in which process the number of ligands is interestingly preserved. The other product of the disproportionation process, *i.e.*, $Au_{40}(TBBT)_{m+2}(SCH_2CH_2Ph)_{24-m}$, was concurrently observed as an intermediate, which was the result of addition of two Au atoms and two TBBT ligands to $Au_{38}(TBBT)_m(SCH_2CH_2Ph)_{24-m}$. The reaction kinetics on the $Au_{38}(SCH_2CH_2Ph)_{24}$ to $Au_{36}(TBBT)_{24}$ conversion process was also performed, and the activation energies of the structural distortion and disproportionation steps were estimated to be 76 and 94 kJ/mol, respectively. The optical absorption features of $Au_{36}(TBBT)_{24}$ are interpreted on the basis of density functional theory simulations.

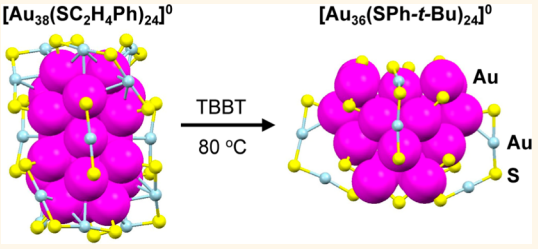

KEYWORDS: gold nanoclusters · ligand-induced transformation · disproportionation mechanism · density functional theory

The synthesis of thiolate-protected gold nanoclusters and studies of their properties have achieved significant advances in recent years.[1−10] A series of atomically precise nanoclusters have been obtained with precise control at the atomic level,[1,2] and well-studied examples include $Au_{25}(SR)_{18}$, $Au_{38}(SR)_{24}$, $Au_{67}(SR)_{35}$, $Au_{102}(SR)_{44}$, $Au_{130}(SR)_{50}$, and $Au_{144}(SR)_{60}$.[1−3,9−24] A few of them have been crystallographically characterized.[8−10,16] Moreover, a size-focusing methodology[24] has been successfully established based upon prior literature work and has been demonstrated to be quite universal,[25−33] giving rise to molecularly pure $Au_{25}(SR)_{18}$, $Au_{38}(SR)_{24}$, and $Au_{144}(SR)_{60}$ nanoclusters[25−27] and bimetal ones,[28−31] as well as some larger nanoclusters.[18,32,33] This methodology comprises two primary steps: (i) kinetically controlled synthesis of a mixture of $Au_n(SR)_m$ with a *properly* controlled size range and (ii) size focusing of the mixture with the controlled size range into single-sized nanoclusters.[24] In addition to the size-focusing method, another useful approach pertains to ligand exchange, such as phosphine-to-thiol exchange processes;[34,35] however, in many cases molecular purity product could not be obtained except in the case of phosphine-capped Au_{11} to thiolate-capped Au_{25}.[34]

The availability of atomically precise nanoclusters opened up new opportunities for ligand exchange synthesis of different sized nanoclusters. We recently performed thiol-to-thiol ligand exchange with 4-*tert*-butylbenzenelthiol (TBBT) using molecularly pure $Au_{38}(PET)_{24}$ nanoclusters (where PET = SCH_2CH_2Ph) as the starting clusters.[36] This process gave rise to a new $Au_{36}(TBBT)_{24}$ nanocluster of molecular purity, and its atomic structure has been successfully solved by single-crystal X-ray crystallography.[36] Interestingly, the structure of $Au_{36}(TBBT)_{24}$ is drastically different from that of the starting $Au_{38}(PET)_{24}$ nanocluster (Scheme 1). The $Au_{38}(PET)_{24}$ nanocluster is intrinsically chiral, and the inner core (*i.e.*, kernel) of both enantiomers consists of a face-sharing biicosahedral Au_{23} unit, which is protected by three $Au(SR)_2$ monomer staples and six $Au_2(SR)_3$ dimer staples.[16] The chirality originates from the dual-propeller-like rotating arrangement of

* Address correspondence to rongchao@andrew.cmu.edu.

Received for review April 19, 2013 and accepted June 4, 2013.

Published online June 12, 2013
10.1021/nn401971g

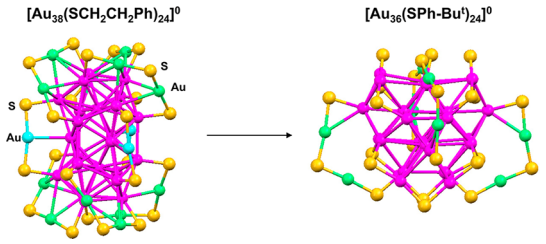

Scheme 1. Conversion of $Au_{38}(PET)_{24}$ to $Au_{36}(TBBT)_{24}$ nanoclusters (the carbon tails are not shown for clarity; S atoms, yellow; kernel Au atoms, magenta; surface Au atoms, green or cyan).

the six dimer staples. By contrast, $Au_{36}(TBBT)_{24}$ is achiral and contains a truncated tetrahedral face-centered-cubic (fcc) Au_{28} kernel.[36] The Au_{28} kernel exposes {111} and {100} facets and is protected by four regular dimer staples and 12 unprecedented, simple bridging thiolates without containing any gold atoms in contrast with $Au(SR)_2$ and $Au_2(SR)_3$ staple motifs. The emergence of an fcc-structured Au_{28} kernel at such a small size was also a surprise, and it breaks the previously thought general trend[37,38] from icosahedral (*e.g.*, $Au_{25}(PET)_{18}$ and $Au_{38}(PET)_{24}$) to decahedral (*e.g.*, $Au_{102}(p\text{-}MBA)_{44}$) to fcc structure in plasmonic nanoparticles[32] and bulk gold.

The transformation of $Au_{38}(SCH_2CH_2Ph)_{24}$ to $Au_{36}(TBBT)_{24}$ nanoclusters is quite remarkable. It raises a number of interesting questions: How does the reaction occur (*i.e.*, the detailed reaction pathway)? Why does the reaction occur (*i.e.*, the driving force leading to the structural transformation)? What specific role does the TBBT ligand play in the process? To address these questions, we are motivated to carry out a detailed investigation of the conversion mechanism. Understanding this ligand-triggered process is important and may lead to the development of another universal methodology for nanocluster synthesis other than the size-focusing methodology.[24]

Herein, we report an interesting disproportionation mechanism identified in the transformation of $Au_{38}(PET)_{24}$ to $Au_{36}(TBBT)_{24}$. Our results indicate that, starting with $Au_{38}(PET)_{24}$, the ligand exchange with bulkier TBBT induces structural distortion of the initial rod-like biicosahedral $Au_{38}(PET)_{24}$ structure. The destabilized structure then spits out two Au atoms and transforms into the tetrahedral $Au_{36}(TBBT)_{24}$ structure (Scheme 1), and concurrently, the released Au atoms combine with $Au_{38}(SR)_{24}$ (where SR includes both PET and TBBT) to form $Au_{40}(SR)_{26}$ in the presence of free TBBT thiol. This process is evidenced by detailed mass spectrometric and optical spectroscopic analyses. The optical spectrum of $Au_{36}(TBBT)_{24}$ was further interpreted by theoretical simulations on a $Au_{36}(SCH_3)_{24}$ model cluster. The electronic transitions and the frontier orbitals were identified.

RESULTS AND DISCUSSION

To study the transformation process, we started with molecularly pure $Au_{38}(PET)_{24}$ with a concentration of 0.16 mg/mL in toluene. Then the $Au_{38}(PET)_{24}$ nanoclusters reacted with excess TBBT thiol under a TBBT/PET ratio of ~160. The reaction was performed at 80 °C, and the reaction mixture was sampled at different time intervals for UV–vis and electrospray ionization mass spectrometry (ESI-MS) analyses (see Supporting Information for details).

Figure 1 shows the ESI-MS and UV–vis spectral evolution of the reaction mixture at different reaction times. In ESI-MS, we used the doubly charged mass peaks for analysis of the species in the reaction mixture due to their higher intensity compared to the singly charged ones (supporting Figure S1). The detailed assignment of peaks is summarized in Table S1 (see Supporting Information). On the basis of the results, the Au_{38} to Au_{36} transformation can be roughly divided into four stages (*vide infra*).

Stage I. In the first stage (0–5 min), ligand exchange reaction occurs. As seen in the ESI-MS spectra, the starting material (*i.e.*, $Au_{38}(PET)_{24}$ nanoclusters) shows a single peak (Figure 1A, 0 min). After 5 min, this peak evolves into a group of peaks with an identical spacing of 14. This spacing corresponds to the mass difference between TBBT and PET ligands (MW of PET = 137 Da, TBBT = 165 Da, $\Delta m/z$ = 14 when z = 2). Thus, this group of peaks can be identified as the TBBT ligand exchange product of $Au_{38}(PET)_{24}$, corresponding to $Au_{38}(TBBT)_m(PET)_{24-m}$. Note that the number on the top of the mass peak indicates the number of TBBT ligands on the nanocluster (for clarity, only one is indicated); up to 12 TBBT ligands were exchanged onto Au_{38} during the first 5 min (Figure 1A).

Concurrently, the UV–vis spectra show no discernible difference between the start and 5 min (Figure 1B). The characteristic peaks of the Au_{38} absorption spectrum are at 490, 620, 750, and 1050 nm (Figure 1B, 0 min).[15,26] These features are well preserved up to 5 min, when a maximum of 12 TBBT ligands are exchanged onto the Au_{38} cluster. The similar absorption spectra indicate that the structure of $Au_{38}(SR)_{24}$ (where SR refers to mixed TBBT and PET) is retaineded during the first ligand exchange process (Scheme 2, stage I). The reaction of this stage can be written as

$$Au_{38}(PET)_{24} + TBBT \rightarrow Au_{38}(TBBT)_m(PET)_{24-m} + PET \quad (m < ca.\ 12) \qquad (1)$$

Stage II. In this stage (10–15 min), the ligand exchange reaction continues, but it starts to induce structural distortion of the original $Au_{38}(SR)_{24}$ cluster, as manifested in the optical spectra. As shown in Figure 1A at t = 10 and 15 min, the number of TBBT ligands further increases in $Au_{38}(TBBT)_m(PET)_{24-m}$ to a maximum of *ca.* 21. Interestingly, a new absorption band at 550 nm appears in the UV–vis spectra (Figure 1B, see the arrow), and its intensity increases as the population of heavily exchanged product

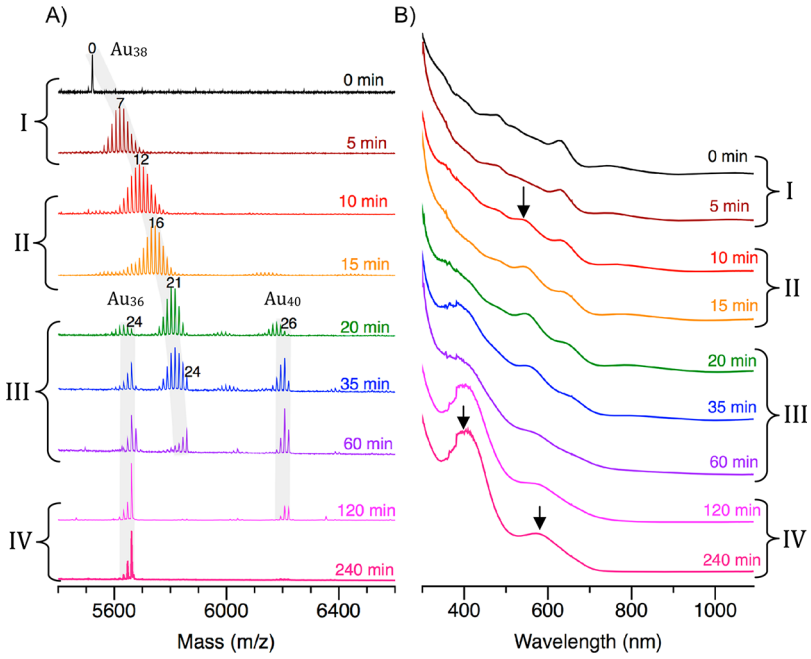

Figure 1. (A) Time-dependent ESI-MS of the transformation reaction. The doubly charged region is shown. The three gray shadows indicate three groups of peaks: (left) $Au_{36}(TBBT)_m(PET)_{24-m}$, (middle) $Au_{38}(TBBT)_m(PET)_{24-m}$, (right) $Au_{40}(TBBT)_{m+2}(PET)_{24-m}$. The numbers on the top of the mass peaks indicate the number of TBBT ligands (m) exchanged onto the cluster. (B) Corresponding UV−vis spectra of different times in parallel with ESI-MS.

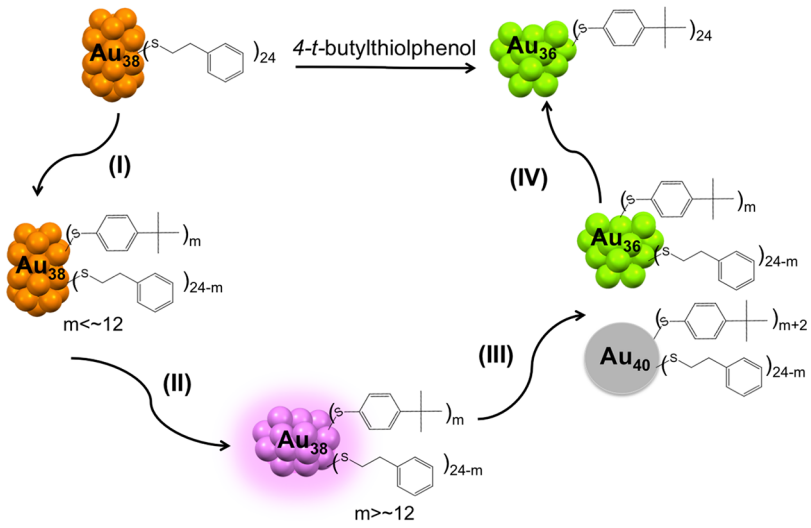

Scheme 2. Reaction pathway for conversion of $Au_{38}(PET)_{24}$ to $Au_{36}(TBBT)_{24}$. Stage I, ligand exchange; II, structure distortion; III, disproportionation; IV, size focusing.

$[Au_{38}(TBBT)_m(PET)_{24-m}]$ increases. The appearance of this 550 nm peak indicates the rearrangement of the $Au_{38}(SR)_{24}$ skeleton; hence the electronic structure of the nanocluster was influenced. This structural distortion should be triggered by the bulkiness of the TBBT ligand, since TBBT is a secondary thiol with its S atom connecting directly to a benzene ring, while PET is a primary thiol with S connecting to a CH_2 group. In order to accommodate more and more bulky TBBT ligands with the ligand exchange reaction going on, the original rod-like structure of $Au_{38}(SR)_{24}$ becomes distorted (Scheme 2, stage II). This structural distortion is the key step for the transformation (size and structural conversions) to occur, entering stage III (*vide infra*). The reaction in this stage can be written as below, with Au_{38}* denoting the distorted structure:

$$Au_{38}(TBBT)_m(PET)_{24-m\ (m<ca.12)} + TBBT \rightarrow Au_{38}{}^*(TBBT)_m(PET)_{24-m\ (m>ca.12)} + PET \quad (2)$$

Stage III. It is in this critical stage (20−60 min) that the size and structural conversions take place. Interestingly, instead of simple conversion from Au_{38}*$(SR)_{24}$

to $Au_{36}(SR)_{24}$, a "disproportionation" reaction is identified: when one Au_{38}*$(SR)_{24}$ cluster releases two gold atoms to form $Au_{36}(SR)_{24}$, another Au_{38}*$(SR)_{24}$ cluster captures the two released gold atoms together with two free TBBT ligands from the solution to form $Au_{40}(SR)_{26}$. This disproportionation process is easily identified in the ESI-MS analysis (Figure 1A, t = 20, 35, 60 min profiles). When t = 20 min, two new sets of peaks with comparable intensities were observed on the left and right sides of the Au_{38}*$(SR)_{24}$ peak set (Figure 1A, t = 20 min). The left set of peaks is identified to be $Au_{36}(TBBT)_m(PET)_{24-m}$ (m = 19 to 24), whereas the right-side set is $Au_{40}(TBBT)_{m+2}(PET)_{24-m}$ (m = 21 to 26). As the reaction continued, the intensity of these Au_{36} and Au_{40} peaks increased, while the intensity of Au_{38} decreased (Figure 1A, t = 35 and 60 min profiles). This trend clearly indicates the transformation of Au_{38}*$(SR)_{24}$ to two products, *i.e.*, $Au_{36}(SR)_{24}$ and $Au_{40}(SR)_{26}$ (Scheme 2). Hence, the reaction in this stage can be written as

$$2Au_{38}{}^*(TBBT)_m(PET)_{24-m} + 2TBBT \rightarrow Au_{36}(TBBT)_m(PET)_{24-m} + Au_{40}(TBBT)_{m+2}(PET)_{24-m} \quad (3)$$

It is worth mentioning that the number of PET ligands in the Au_{36}, Au_{38}* and Au_{40} nanoclusters is roughly conserved when the disproportionation reaction first takes place: all ranging from 0 to 6 with maximum at ~3. The unexchanged PET ligands actually act as a label for the ligand shell of the three clusters. The conservation of PET ligands in these three clusters indicates the transformation reaction was achieved within the original cluster *via internal reconstruction* (as opposed to complete disintegration followed by reassembly of pieces), and simple releasing and capturing processes lead to the formation of new Au_{36} and Au_{40} clusters. Another note is that tiny amounts of $Au_{39}(SR)_{25}$ and $Au_{41}(SR)_{27}$ were also observed in the ESI-MS spectra (see Supporting Figure S2, zoom-in mass spectrum for t = 35 min), indicating that the capturing of released gold atoms and free TBBT ligands by Au_{38}*$(SR)_{24}$ progresses one by one, but the stability of $Au_{39}(SR)_{25}$ and $Au_{41}(SR)_{27}$ is less than that of $Au_{40}(SR)_{26}$ since the latter was much more abundant.

The characteristic absorption peaks of $Au_{36}(SR)_{24}$ are at 380 and 570 nm.[36] As shown in Figure 1B (profiles 20, 35, 60 min), a hump first appeared at 380 nm and its intensity gradually increased, corresponding to the increasing abundance of Au_{36}. The decreasing intensity of the afore-discussed 550 nm peak within 20–65 min is consistent with the trend of decreasing abundance of Au_{38}*$(TBBT)_m(PET)_{24-m}$ species in the ESI-MS.

Stage IV. After all the Au_{38}*$(TBBT)_m(PET)_{24-m}$ are transformed into $Au_{36}(TBBT)_m(PET)_{24-m}$ and $Au_{40}(TBBT)_{m+2}(PET)_{24-m}$ (Figure 1A, t = 120 min), evidenced by the complete disappearance of the Au_{38}*$(TBBT)_m(PET)_{24-m}$ peak set, the reaction enters the fourth stage (120–300 min), during which a size focusing conversion occurs together with further ligand exchange toward completion (*i.e.*, until 24 TBBT ligands). As shown in the 120 min profile, the intensity of $Au_{40}(TBBT)_{m+2}(PET)_{24-m}$ becomes significantly lower than that of $Au_{36}(TBBT)_m(PET)_{24-m}$, indicating that Au_{40} is somewhat less stable than Au_{36} under the harsh environment of high temperature and excess thiol, while $Au_{36}(SR)_{24}$ survives due to its extraordinary stability.

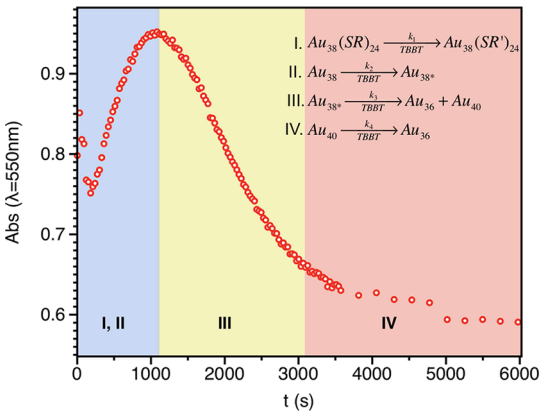

Figure 2. Kinetic curve (monitored by absorbance at 550 nm) for the conversion of $Au_{38}(PET)_{24}$ to $Au_{36}(TBBT)_{24}$ at 80 °C.

An interesting question pertains to the ultimate fate of $Au_{40}(SR)_{26}$. Does it decompose to Au(I)-SR polymer or convert to $Au_{36}(SR)_{24}$? If $Au_{40}(SR)_{26}$ decomposes, the final $Au_{36}(SR)_{24}$ yield would be ~47% (gold atom basis) according to the disproportionation (eq 3) (see above, *i.e.* 36/(2 × 38) = 0.47). On the other hand, if $Au_{40}(SR)_{26}$ eventually converts to $Au_{36}(SR)_{24}$,

$$Au_{40}(SR)_{26} \rightarrow Au_{36}(SR)_{24} + 2Au(0) + 2Au(I)SR \quad (4)$$

then the yield of final $Au_{36}(SR)_{24}$ would be doubled (~94%), as eq 4 combined with eq 3 gives an overall equation:

$$\begin{aligned} 2Au_{38}(SR)_{24} + 2TBBT &\rightarrow Au_{40}(SR)_{26} + Au_{36}(SR)_{24} \\ Au_{40}(SR)_{26} &\rightarrow Au_{36}(SR)_{24} + 2Au(0) + 2Au(I)SR \\ \text{Overall}: \quad 2Au_{38}(SR)_{24} &\rightarrow 2Au_{36}(SR)_{24} + 2Au(0) \end{aligned} \quad (5)$$

To answer the question, we determined the reaction yield of $Au_{36}(SR)_{24}$, which is ~90%, close to the expected yield according to eq 5; hence the Au_{40} product is eventually converted to Au_{36} clusters during the third and fourth stages, instead of decomposing to Au(I)-SR polymer. The reaction is completed when the last PET ligand on Au_{36} is exchanged by TBBT (Scheme 2). Futher heating of the $Au_{36}(TBBT)_{24}$ clusters under excess TBBT ligand does not cause any further changes; therefore $Au_{36}(TBBT)_{24}$ is an extremely stable species.

Kinetics of the Conversion Process. The 550 nm peak can be used for the kinetic study. Figure 2 shows the evolution of the 550 nm peak as a function of time with the reaction carried out at 80 °C. The increase in intensity during ~200 to ~1000 s implies the

increasing amount of Au_{38}* formed during the ligand-induced structural distortion process (*i.e.*, stage II), while the decreasing intensity over the ~1000 to ~3000 s period is mainly due to the transformation of Au_{38}* into Au_{36} and Au_{40} (*i.e.*, stage III). Of note, the decrease of intensity in the first ~200 s is caused by the turbulence of the solution during heating from RT to 80 °C, and the initial ligand exchange stage shows no absorbance change; thus the rate constant cannot be determined. Herein we focus only on stages II and III. By taking a first-order kinetic model, we obtained rate constants (k_2 and k_3) at 60, 70, and 80 °C (Table 1). By plotting $\ln(k_{2\text{ or }3})$ against $1/T$, the activation energy (E_a) is obtained; for stage II, $E_{a,II}$ is ~107 kJ/mol, and for stage III, $E_{a,III}$ is ~152 kJ/mol (for details see the Supporting Information). The kinetics for stage IV was not pursued due to the least absorbance changes and large noise. It should be noted that our kinetics analysis is only semiquantitative, as the four stages cannot be completely separated.

Steric Hindrance and Electronic Conjugation Effects of the TBBT Ligand. It is interesting to know why the TBBT ligand can be used to synthesize a new gold nanocluster different from the well-known "magic sizes" such as $Au_{25}(SR)_{18}$, $Au_{38}(SR)_{24}$, and $Au_{102}(SR)_{44}$. The main differences between TBBT and alkyl-chain thiolate (such as HS-*n*-C_6H_{13} and PET) lie in that (i) TBBT is much bulkier since it is a secondary thiol and (ii) the sulfur atom is conjugated with the aromatic ring. To test the potential roles of steric hindrance and electronic conjugation of TBBT in the synthesis of $Au_{36}(TBBT)_{24}$, we choose a cyclohexanethiol ligand, which is similar in bulkiness to TBBT but without an aromatic ring. The transformation reaction was done with all the conditions kept the same (*e.g.*, thiol/Au_{38} ratio, temperature) except the thiol type. The time-dependent UV–vis spectra were recorded to monitor the reaction process and compared with the TBBT case (Figure 3A,B). Interestingly, we also observed that a new peak around 530 nm appeared first (Figure 3B) and then disappeared during the reaction of cyclohexanethiol with $Au_{38}(PET)_{24}$, which is very similar to the stage II and III of TBBT as aforediscussed. Thus, the new absorption band and its implications are common in both reactions of cyclohexanecethiol and TBBT, indicating that it is the *bulkiness* of the ligand that triggers the initial transformation process due to distortion to the original Au_{38} structure. It is worth mentioning that bulky ligands were found to have large effects on cluster size.[4,5] In our system, the final product of cyclohexanethiol exchange however shows a featureless optical spectrum (Figure 3B, blue profile), rather than a distinct spectrum as in the case of TBBT; the former implies a possible mixture of different sizes, which is indeed confirmed by ESI-MS analysis (supporting Figure S3). This is in striking contrast with the *exclusive* formation of $Au_{36}(TBBT)_{24}$ in the case of TBBT. The result of the cyclohexanethiol exchange process implies that the conjugation effect of the aromatic TBBT ligand is also important for exclusive formation and stabilization of $Au_{36}(SR)_{24}$ since other sizes as in cyclohexanethiol exchange are not observed. Taken together, both the steric bulkiness and electronic conjugation factors of TBBT are important for the successful transformation from $Au_{38}(SR)_{24}$ to very clean $Au_{36}(TBBT)_{24}$ in high yield (~90%, approaching the theoretical 94% yield as indicated by the overall reaction, eq 5).

Interpretation of the Optical Spectrum. We further interpret the optical absorption features of $Au_{36}(SR)_{24}$ by performing time-dependent density functional theory (TD-DFT) simulations. DFT optimizations of the $Au_{36}(SR)_{24}$ (R is simplified as a methyl group) are performed using the generalized gradient approximation with the Perdew–Burke–Ernzerhof functional combined with the triple-ζ polarized (TZP) basis set with inclusion of scalar relativistic effects *via* zeroth-order regular approximation implemented in the Amsterdam Density Functional package.[39,40] The TD-DFT computation of the optical absorption spectrum is performed at the LB94/TZP

TABLE 1. Rate Constants for Stages II and III at Different Reaction Temperatures

	60 °C	70 °C	80 °C
$k_{2,obs}$ (s^{-1})	4.0×10^{-4}	1.4×10^{-3}	3.5×10^{-3}
$k_{3,obs}$ (s^{-1})	4.8×10^{-5}	1.8×10^{-4}	1.1×10^{-3}

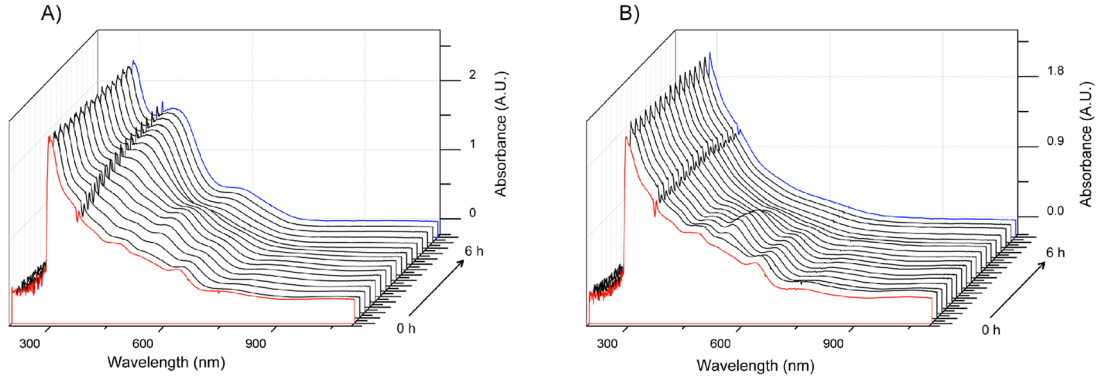

Figure 3. Time-dependent UV–vis spectral evolution of (A) 4-*tert*-butylbenzenethiol and (B) cyclohexanethiol reaction with $Au_{38}(PET)_{24}$.

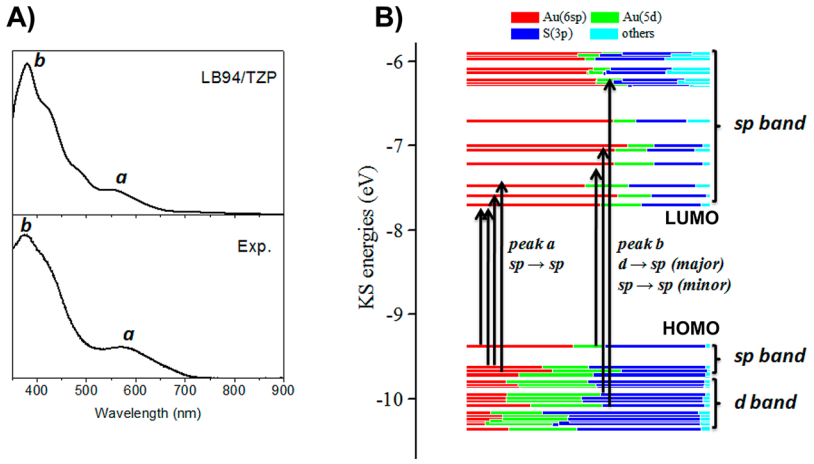

Figure 4. (A) Comparison of simulated UV−vis absorption spectrum of $Au_{36}(SR)_{24}$ with the experimental spectrum. (B) Estimation of contributions of Au(6sp), Au(5d), and S(3p) to KS orbitals.

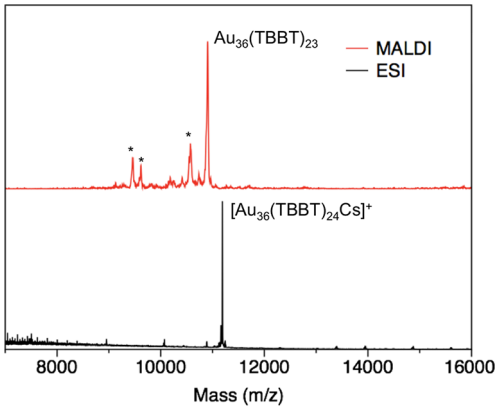

Figure 5. Comparison of the MALDI-MS and ESI-MS spectra of $Au_{36}(TBBT)_{24}$. The asterisks indicate the fragments due to MALDI.

level of theory with the lowest 200 singlet-to-singlet excitation energies computed, similar to previous works.[41−44]

The theoretical optical adsorption spectrum agrees well with the experimental measurement (Figure 4A). On the basis of computed excitation energies and Kohn−Sham (KS) orbitals, we have assigned the orbital transition modes of two distinct adsorption peaks (*a* and *b*) observed in the experiment (Figure 4B). Peak *a* is contributed primarily from the HOMO to LUMO transition, with some minor contributions from the transition of electrons from lower energy orbitals (HOMO−*n*) to the LUMO and higher unoccupied orbitals. For peak *b*, the transition of electrons from the HOMO to higher unoccupied orbitals is observed. With respect to the atomic orbital compositions of the KS orbitals (Figure 4B), the HOMO−3 to HOMO, as well as LUMO and above, are all mainly composed of Au(6sp) atomic orbitals (highlighted in red), denoted as the sp band, while the HOMO−4 and lower orbitals form the d band since they are mainly contributed by Au(5d).

Comparison of MALDI-MS and ESI-MS Characterization. Herein it is worth commenting on the matrix-assisted laser ionization mass spectrometry (MALDI-MS) characterization of $Au_{36}(TBBT)_{24}$. In the MALDI mass spectrum of $Au_{36}(TBBT)_{24}$ nanoclusters, we did not observe the *intact* cluster ions but the one-ligand-lost product, $Au_{36}(TBBT)_{23}$ (Figure 5), reminiscent of the $Au_{36}(SPh)_{23}$ species reported previously by Dass and co-workers using MALDI-MS analysis.[45] Thus, $Au_{36}(TBBT)_{23}$ is an artifact due to MALDI-MS since the $Au_{36}(TBBT)_{24}$ formula has been unambiguously established by ESI-MS and X-ray crystallography.[36] MALDI-MS is being widely used, and the majority of cases give reliable information,[46−50] but an ESI-MS double check is highly desirable.

CONCLUSION

We have elucidated the detailed mechanism of the ligand-induced conversion from $Au_{38}(PET)_{24}$ to $Au_{36}(TBBT)_{24}$. The reaction pathway can be roughly divided into four stages: (I) PET to TBBT ligand exchange, (II) TBBT-triggered structural distortion of Au_{38} with an optical feature at 550 nm, (III) disproportionation of Au_{38} to Au_{36} and Au_{40}, and (IV) size conversion of Au_{40} to Au_{36}. This process gave rise to Au_{36} nanoclusters in a ~90% yield (Au atom basis), approaching the theoretical yield of ~94% according to the disproportionation mechanism. The conversion of biicosahedral Au_{38} structure to fcc Au_{36} structure is remarkable; it provides an unprecedented example of ligand bulkiness induced size and structural transformation in thiolate-protected nanoclusters.

METHODS

Chemicals. Tetrachloroauric(III) acid ($HAuCl_4 \cdot 3H_2O$, >99.99% metals basis, Aldrich), 2-phenylethanethiol (PET, 99%, Acros Organics), glutathione (G-SH, 98%, Acros Organics), sodium borohydride ($NaBH_4$, Aldrich), 4-*tert*-butylbenzenethiol (TBBT, 97%, Alfa Aesar), and cyclohexanethiol (97%, Aldrich) were used. Solvents used were methanol (HPLCgrade, ≥99.9%,

Aldrich), ethanol (absolute, 200 proof, Pharmco), dimethylene chloride (HPLC grade, ≥99.9%, Aldrich), and toluene (HPLC grade, 99.9%, Aldrich). All chemicals were used as received.

Experiment. The synthesis of $Au_{38}(PET)_{24}$ (PET: SCH_2CH_2Ph) was based on a previously reported size focusing method.[26] To study the transformation process, we first dissolved $Au_{38}(PET)_{24}$ single crystals in toluene to make a solution of 0.16 mg/mL (absorbance at 626 nm λ_{626} = 0.616 OD); note that the extinction coefficiency of $Au_{38}(PET)_{24}$ at 626 nm is $\varepsilon_{626} = 4.2 \times 10^4\ M^{-1}\ cm^{-1}$ in toluene. Then, 4-*tert*-butylbenzenethiol was added to the $Au_{38}(PET)_{24}$ solution. The molar ratio of TBBT to PET (in $Au_{38}(PET)_{24}$) was kept at ~160. The mixture was heated to 80 °C under magnetic stirring in an air atmosphere. Approximately 1 mL of solution was sampled at different time intervals and cooled immediately. The sample was then directly subjected to UV−vis analysis. Then the solvent (toluene) was removed by rotary evaporation, and 1 mL of methanol was added. The gold nanoclusters precipitated out after centrifugation at 10 000 rpm for 5 min. The supernatant (containing excess TBBT) was discarded. The precipitate was subjected to washing with methanol three times to make sure no TBBT remained. Once separated from TBBT, the gold nanoclusters were stable (*i.e.*, without further reactions with TBBT). The as-collected nanoclusters were then characterized by ESI-MS.

In kinetics measurements, 1 mL of a toluene solution of $Au_{38}(PET)_{24}$ in a 1 cm quartz cuvette (absorbance at 550 nm ~0.75 OD) was mixed with 10 μL of TBBT. The kinetics was carried out using a Hewlett-Packard (HP) Agilent 8453 diode array spectrophotometer equipped with an HP 89090A Peltier temperature controller. The cuvette was placed in the sample holder preset at 60, 70, or 80 °C, with constant magnetic stirring (500 rmp), and the UV−vis absorption spectra were recorded with time. The temporal change of absorbance at 550 nm was used for kinetic analysis.

Characterization. UV−vis spectra of the Au clusters were acquired on an HP Agilent 8453 diode array spectrophotometer at room temperature. ESI-MS were recorded using a Waters Q-TOF mass spectrometer equipped with Z-spray source. The source temperature was kept at 70 °C. The sample was directly infused into the chamber at 5 μL/min. The spray voltage was kept at 2.20 kV, and the cone voltage at 60 V. The ESI sample was dissolved in toluene (~1 mg/mL) and diluted (1:2 v/v) by dry methanol (containing 50 mM CsOAc to enhance cluster ionization in ESI).

Conflict of Interest: The authors declare no competing financial interest.

Acknowledgment. Y.P. acknowledges financial support by the Natural Science Foundation of China (Grant No. 21103144) and Hunan Provincial Natural Science Foundation of China (12JJ7002, 12JJ1003). R.J. acknowledges support by the Air Force Office of Scientific Research under AFOSR Award No. FA9550-11-1-9999 (FA9550-11-1-0147) and the Camille Dreyfus Teacher-Scholar Awards Program. We thank Dr. Zhongrui Zhou for assistance in ESI-MS analysis and Dr. Huifeng Qian for valuable discussions.

Supporting Information Available: Full-range ESI-MS spectra (Figure S1), detailed ESI-MS peak assignment (Table S1), zoom-in ESI-MS (Figure S2), ESI-MS of the final product of Au_{38} reacting with cyclohexanethiol (Figure S3), and kinetics and activation energy analysis (Figures S4−S6). This material is available free of charge *via* the Internet at http://pubs.acs.org.

REFERENCES AND NOTES

1. Qian, H.; Zhu, M.; Wu, Z.; Jin, R. Quantum Sized Gold Nanoclusters with Atomic Precision. *Acc. Chem. Res.* **2012**, *45*, 1470–1479.
2. Maity, P.; Xie, S.; Yamauchi, M.; Tsukuda, T. Stabilized Gold Clusters: From Isolation toward Controlled Synthesis. *Nanoscale* **2012**, *4*, 4027–4037.
3. Zheng, J.; Zhou, C.; Yu, M.; Liu, J. Different Sized Luminescent Gold Nanoparticles. *Nanoscale* **2012**, *4*, 4073–4083.
4. Nishigaki, J.-i.; Tsunoyama, R.; Tsunoyama, H.; Ichikuni, N.; Yamazoe, S.; Negishi, Y.; Ito, M.; Matsuo, T.; Tamao, K.; Tsukuda, T. A New Binding Motif of Sterically Demanding Thiolates on a Gold Cluster. *J. Am. Chem. Soc.* **2012**, *134*, 14295–14297.
5. Krommenhoek, P. J.; Wang, J.; Hentz, N.; Johnston-Peck, A. C.; Kozek, K. A.; Kalyuzhny, G.; Tracy, J. B. Bulky Adamantanethiolate and Cyclohexanethiolate Ligands Favor Smaller Gold Nanoparticles with Altered Discrete Sizes. *ACS Nano* **2012**, *6*, 4903–4911.
6. Dass, A.; Holt, K.; Parker, J. F.; Feldberg, S. W.; Murray, R. W. Mass Spectrometrically Detected Statistical Aspects of Ligand Populations in Mixed Monolayer $Au_{25}L_{18}$ Nanoparticles. *J. Phys. Chem. C* **2008**, *112*, 20276–20283.
7. Muhammed, M. A. H.; Verma, P. K.; Pal, S. K.; Kumar, R. C. A.; Paul, S.; Omkumar, R. V.; Pradeep, T. Bright, NIR-Emitting Au_{23} from Au_{25}: Characterization and Applications Including Biolabeling. *Chem.—Eur. J.* **2009**, *15*, 10110–10120.
8. Jadzinsky, P. D.; Calero, G.; Ackerson, C. J.; Bushnell, D. A.; Kornberg, R. D. Structure of a Thiol Monolayer-Protected Gold Nanoparticle at 1.1 Å Resolution. *Science* **2007**, *318*, 430–433.
9. Zhu, M.; Aikens, C. M.; Hollander, F. J.; Schatz, G. C.; Jin, R. Correlating the Crystal Structure of A Thiol-Protected Au_{25} Cluster and Optical Properties. *J. Am. Chem. Soc.* **2008**, *130*, 5883–5885.
10. Heaven, M. W.; Dass, A.; White, P. S.; Holt, K. M.; Murray, R. W. Crystal Structure of the Gold Nanoparticle $[N(C_8H_{17})_4][Au_{25}(SCH_2CH_2Ph)_{18}]$. *J. Am. Chem. Soc.* **2008**, *130*, 3754–3755.
11. Heinecke, C. L.; Ni, T. W.; Malola, S.; Mäkinen, V.; Wong, O. A.; Häkkinen, H.; Ackerson, C. J. Structural and Theoretical Basis for Ligand Exchange on Thiolate Monolayer Protected Gold Nanoclusters. *J. Am. Chem. Soc.* **2012**, *134*, 13316–13322.
12. Negishi, Y.; Kurashige, W.; Kamimura, U. Isolation and Structural Characterization of an Octaneselenolate-Protected Au_{25} Cluster. *Langmuir* **2011**, *27*, 12289–12292.
13. Meng, X.; Xu, Q.; Wang, S.; Zhu, M. Ligand-Exchange Synthesis of Selenophenolate-Capped Au_{25} Nanoclusters. *Nanoscale* **2012**, *4*, 4161–4165.
14. Negishi, Y.; Chaki, N. K.; Shichibu, Y.; Whetten, R. L.; Tsukuda, T. Origin of Magic Stability of Thiolated Gold Clusters: A Case Study on $Au_{25}(SC_6H_{13})_{18}$. *J. Am. Chem. Soc.* **2007**, *129*, 11322–11323.
15. Chaki, N. K.; Negishi, Y.; Tsunoyama, H.; Shichibu, Y.; Tsukuda, T. Ubiquitous 8 and 29 kDa Gold:Alkanethiolate Cluster Compounds: Mass-Spectrometric Determination of Molecular Formulas and Structural Implications. *J. Am. Chem. Soc.* **2008**, *130*, 8608–8610.
16. Qian, H.; Eckenhoff, W. T.; Zhu, Y.; Pintauer, T.; Jin, R. Total Structure Determination of Thiolate-Protected Au_{38} Nanoparticles. *J. Am. Chem. Soc.* **2010**, *132*, 8280–8281.
17. Nimmala, P. R.; Yoon, B.; Whetten, R. L.; Landman, U.; Dass, A. $Au_{67}(SR)_{35}$ Nanomolecules: Characteristic Size-Specific Optical, Electrochemical, Structural Properties and First-Principles Theoretical Analysis. *J. Phys. Chem. A* **2013**, *117*, 504–517.
18. Negishi, Y.; Sakamoto, C.; Ohyama, T.; Tsukuda, T. Synthesis and the Origin of the Stability of Thiolate-Protected Au_{130} and Au_{187} Clusters. *J. Phys. Chem. Lett.* **2012**, *3*, 1624–1628.
19. Tang, Z.; Robinson, D. A.; Bokossa, N.; Xu, B.; Wang, S.; Wang, G. Mixed Dithiolate Durene-DT and Monothiolate Phenylethanethiolate Protected Au_{130} Nanoparticles with Discrete Core and Core-Ligand Energy States. *J. Am. Chem. Soc.* **2011**, *133*, 16037–16044.
20. Shibu, E. S.; Radha, B.; Verma, P. K.; Bhyrappa, P.; Kulkarni, G. U.; Pal, S. K.; Pradeep, T. Functionalized Au_{22} Clusters: Synthesis, Characterization, and Patterning. *ACS Appl. Mater. Interfaces* **2009**, *1*, 2199–2210.
21. Wang, M.; Wu, Z.; Yang, J.; Wang, G.; Wang, H.; Cai, W. $Au_{25}(SG)_{18}$ as a Fluorescent Iodide Sensor. *Nanoscale* **2012**, *4*, 4087–4090.
22. Zhu, M.; Qian, H.; Jin, R. Thiolate-Protected $Au_{24}(SC_2H_4Ph)_{20}$ Nanoclusters: Superatoms or Not? *J. Phys. Chem. Lett.* **2010**, *1*, 1003–1007.

23. Yuan, X.; Yu, Y.; Yao, Q.; Zhang, Q.; Xie, J. Fast Synthesis of Thiolated Au_{25} Nanoclusters *via* Protection−Deprotection Method. *J. Phys. Chem. Lett.* **2012**, *3*, 2310–2314.
24. Jin, R.; Qian, H.; Wu, Z.; Zhu, Y.; Zhu, M.; Mohanty, A.; Garg, N. Size Focusing: A Methodology for Synthesizing Atomically Precise Gold Nanoclusters. *J. Phys. Chem. Lett.* **2010**, *1*, 2903–2910.
25. Wu, Z.; Suhan, J.; Jin, R. One-Pot Synthesis of Atomically Monodisperse, Thiol-Functionalized Au_{25} Nanoclusters. *J. Mater. Chem.* **2009**, *19*, 622–626.
26. Qian, H.; Zhu, Y.; Jin, R. Size-Focusing Synthesis, Optical and Electrochemical Properties of Monodisperse $Au_{38}(SC_2H_4Ph)_{24}$ Nanoclusters. *ACS Nano* **2009**, *3*, 3795–3803.
27. Qian, H.; Jin, R. Controlling Nanoparticles with Atomic Precision: The Case of $Au_{144}(SCH_2CH_2Ph)_{60}$. *Nano Lett.* **2009**, *9*, 4083–4087.
28. Negishi, Y.; Kurashige, W.; Niihori, Y.; Iwasa, T.; Nobusada, K. Isolation, Structure, and Stability of a Dodecanethiolate-Protected Pd_1Au_{24} Cluster. *Phys. Chem. Chem. Phys.* **2010**, *12*, 6219–6225.
29. Christensen, S. L.; MacDonald, M. A.; Chatt, A.; Zhang, P.; Qian, H.; Jin, R. Dopant Location, Local Structure, and Electronic Properties of $Au_{24}Pt(SR)_{18}$ Nanoclusters. *J. Phys. Chem. C* **2012**, *116*, 26932–26937.
30. Kumara, C.; Dass, A. $(AuAg)_{144}(SR)_{60}$ Alloy Nanomolecules. *Nanoscale* **2011**, *3*, 3064–3067.
31. Negishi, Y.; Igarashi, K.; Munakata, K.; Ohgakea, W.; Nobusada, K. Palladium Doping of Magic Gold Cluster $Au_{38}(SC_2H_4Ph)_{24}$: Formation of $Pd_2Au_{36}(SC_2H_4Ph)_{24}$ with Higher Stability than $Au_{38}(SC_2H_4Ph)_{24}$. *Chem. Commun.* **2012**, *48*, 660–662.
32. Qian, H.; Zhu, Y.; Jin, R. Atomically Precise Gold Nanocrystal Molecules with Surface Plasmon Resonance. *Proc. Natl. Acad. Sci. U.S.A.* **2012**, *109*, 696–670.
33. Dass, A. Faradaurate Nanomolecules: A Superstable Plasmonic 76.3 kDa Cluster. *J. Am. Chem. Soc.* **2011**, *133*, 19259–19261.
34. Shichibu, Y.; Negishi, Y.; Tsukuda, T.; Teranishi, T. Large-Scale Synthesis of Thiolated Au_{25} Clusters *via* Ligand Exchange Reactions of Phosphine-Stabilized Au_{11} Clusters. *J. Am. Chem. Soc.* **2005**, *127*, 13464–13465.
35. Balasubramanian, R.; Guo, R.; Mills, A. J.; Murray, R. W. Reaction of $Au_{55}(PPh_3)_{12}Cl_6$ with Thiols Yields Thiolate Monolayer Protected Au_{75} Clusters. *J. Am. Chem. Soc.* **2005**, *127*, 8126–8132.
36. Zeng, C.; Qian, H.; Li, T.; Li, G.; Rosi, N. L.; Yoon, B.; Barnett, R. N.; Whetten, R. L.; Landman, U.; Jin, R. Total Structure and Electronic Properties of the Gold Nanocrystal $Au_{36}(SR)_{24}$. *Angew. Chem., Int. Ed.* **2012**, *51*, 13114–13118.
37. Cleveland, C. L.; Landman, U.; Schaaff, T. G.; Shafigullin, M. N.; Stephens, P. W.; Whetten, R. L. Structural Evolution of Smaller Gold Nanocrystals: The Truncated Decahedral Motif. *Phys. Rev. Lett.* **1997**, *79*, 1873–1876.
38. Jin, R.; Zhu, Y.; Qian, H. Quantum-Sized Gold Nanoclusters: Bridging the Gap between Organometallics and Nanocrystals. *Chem.—Eur. J.* **2011**, *17*, 6584–6593.
39. *ADF 2010.01*; SCM, Theoretical Chemistry, Vrije Universiteit: Amsterdam, The Netherlands (http://www.scm.com).
40. Perdew, J. P.; Burke, K.; Ernzerhof, M. Generalized Gradient Approximation Made Simple. *Phys. Rev. Lett.* **1996**, *77*, 3865–3868.
41. Pei, Y.; Zeng, X. C. Investigating the Structural Evolution of Thiolate Protected Gold Clusters from First-Principles. *Nanoscale* **2012**, *4*, 4054–4072.
42. Pei, Y.; Gao, Y.; Zeng, X. C. Structural Prediction of Thiolate-Protected Au_{38}: A Face-Fused Bi-icosahedral Au Core. *J. Am. Chem. Soc.* **2008**, *130*, 7830–7832.
43. Pei, Y.; Pal, R.; Liu, C.; Gao, Y.; Zhang, Z.; Zeng, X. C. Interlocked Catenane-like Structure Predicted in $Au_{24}(SR)_{20}$: Implication to Structural Evolution of Thiolated Gold Clusters from Homoleptic Gold(I) Thiolates to Core-Stacked Nanoparticles. *J. Am. Chem. Soc.* **2012**, *134*, 3015–3024.
44. Jiang, D. The Expanding Universe of Thiolated Gold Nanoclusters and Beyond. *Nanoscale* **2013**, DOI: 10.1039/C3NR34192E.
45. Nimmala, P. R.; Dass, A. $Au_{36}(SPh)_{23}$ Nanomolecules. *J. Am. Chem. Soc.* **2011**, *133*, 9175–9177.
46. Dass, A.; Stevenson, A.; Dubay, G. R.; Tracy, J. B.; Murray, R. W. Nanoparticle MALDI-TOF Mass Spectrometry without Fragmentation: $Au_{25}(SCH_2CH_2Ph)_{18}$ and Mixed Monolayer $Au_{25}(SCH_2CH_2Ph)_{18-x}(L)_x$. *J. Am. Chem. Soc.* **2008**, *130*, 5940–5946.
47. Knoppe, S.; Dharmaratne, A. C.; Schreiner, E.; Dass, A.; Bürgi, T. Ligand Exchange Reactions on Au_{38} and Au_{40} Clusters: A Combined Circular Dichroism and Mass Spectrometry Study. *J. Am. Chem. Soc.* **2010**, *132*, 16783–16789.
48. Niihori, Y.; Matsuzaki, M.; Pradeep, T.; Negishi, Y. Separation of Precise Compositions of Noble Metal Clusters Protected with Mixed Ligands. *J. Am. Chem. Soc.* **2013**, *135*, 4946–4949.
49. Tsunoyama, R.; Tsunoyama, H.; Pannopard, P.; Limtrakul, J.; Tsukuda, T. MALDI Mass Analysis of 11 kDa Gold Clusters Protected by Octadecanethiolate Ligands. *J. Phys. Chem. C* **2010**, *114*, 16004–16009.
50. Qian, H.; Jin, R. Synthesis and Electrospray Mass Spectrometry Determination of Thiolate-Protected $Au_{55}(SR)_{31}$ Nanoclusters. *Chem. Commun.* **2011**, *47*, 11462–11464.